

# Computational Analysis of the Flow in the Left Coronary Arteries: Influence of the Artery Elasticity and the Stent Presence in Blood Flow

Bernardo de Sousa Lopes Diogo  
bernardo.diogo@tecnico.ulisboa.pt

Instituto Superior Técnico, Universidade de Lisboa, Portugal

June 2017

## Abstract

CFD blood flow simulations are increasingly used in combination with patient-specific models, constituting a non-invasive method, with lower costs than the experimental procedures used. One major advantage is the possibility of obtaining distributions of parameters such as wall shear stress (WSS), which otherwise are very difficult to obtain. In this work, the fluid-structure interaction problem of blood flow is analyzed in a 3D model of real left coronary arteries geometry, obtained with medical image segmentation. Firstly, blood flow in arteries in normal conditions is analyzed in detail, with emphasis on pressure, velocity, wall shear stress, and displacement. Changes in the flow caused by a stenosis are verified, and the influence of the typical solution for this medical condition, the placement of a stent, on blood flow is also analyzed. The elasticity of the arteries is a parameter that must be taken into account, with significant displacement being verified during the cardiac cycle. It is observed that the stenosis significantly alters the flow locally, with the appearance of low-velocity recirculation zones downstream, which contribute to the spreading of atherosclerosis plaque. It is also concluded that the presence of the stent changes the flow locally, namely near the wall.

**Keywords:** Blood flow, CFD, Fluid-structure interaction, Patient-specific model, Stent

## 1. Introduction

The leading cause of death nowadays is cardiovascular disease, being coronary artery disease (CAD) the one that causes more deaths. It is estimated that in 2015 17.9 million people (32.12% of the total deaths) died due to cardiovascular diseases, of which 8.9 million (15.98% of the total deaths) died due to coronary heart disease [1]. With so many deaths occurring due to cardiovascular diseases it is important to study the cardiovascular system and its most common disorders and this is where computational blood flow simulations become relevant. The importance of the computational simulation of the cardiovascular system is evidenced by being considered one of the most important challenges in the interface between engineering and medicine [2].

The use of computational fluid dynamics (CFD) is becoming more frequent in the biomedical field, with emphasis on the cardiovascular system. This is due to the increased reliability and accessibility of the commercial codes, together with the reduction of hardware costs and increase of the computational power available. However, the advances in the use of CFD to simulate blood flow would not be possible

if they had not been accompanied by a development of medical imaging techniques that allow obtaining realistic geometries [3, 4, 5].

One advantage of using CFD to simulate the cardiovascular system and its diseases is its non-invasive nature. Another advantage is the reduction of costs and time, compared to traditional methods. It allows obtaining results, such as wall shear stress (WSS) distribution, which is a very important factor in the development of atherosclerosis for example. Otherwise, these parameters are obtained with great difficulty, using invasive methods. Another field where the use of CFD is advantageous is the design and optimisation of medical devices such as valves, stents and prostheses, with rapid prototype development and risk reduction for humans [4].

The tissues of the heart, as with any other organ, also need to be supplied with oxygen-rich blood. This is the function of the coronary circulation, the perfusion of the heart, with a large part of the coronary blood vessels embedded in the myocardium [6]. Coronary flow represents about 4% of the total cardiac output [7]. The root of the coronary arterial tree is just above the aortic valve, with the left and

right main coronary arteries originating from the top of a structure called sinus of Valsalva. The left main coronary artery (LCA) gives rise to two major branches, the left descending artery (LAD) and left circumflex artery (LCX) and they and their respective branches distribute blood to the left side of the heart, atrium and ventricle, and the interventricular septum, which separates both ventricles. The right coronary artery (RCA) and its branches distribute blood to the right side of the heart, atrium and ventricle, and usually to a portion of the left ventricle too [8, 9]. There has been some research on coronary flow, most with simpler geometries, such as Torii et al. [10], where blood flow is simulated in a realistic geometry of a section of a stenosed RCA. As boundary conditions, a velocity waveform in the proximal RCA and a pressure waveform in the distal RCA were imposed and a comparison between fluid-structure interaction (FSI) and rigid wall was performed. A more comprehensive study was performed in Kim et al. [7], with a more complete and realistic coronary geometry, including branches of LAD, LCX and RCA. In this study coronary flow was predicted instead of imposed, with coupling between 3D simulation of the flow in the coronaries, in the aorta and in the beginning of the aortic arch branches and reduced order models as boundary conditions simulating the systemic and pulmonary circulation, including a model of the heart. Regarding wall behaviour, FSI methodology was used.

Coronary heart disease is actually a set of diseases, the major cause of which is coronary atherosclerosis. Atherosclerosis is an inflammatory process that results from chronic injury to the blood vessel wall and leads to the formation of atheromatous plaques. These plaques tend to accumulate in regions with low velocities and shear stresses, typically lying near bifurcations. In the coronary arteries, this plaque accumulation occurs mainly in the proximal LAD and the proximal and distal RCA. The main consequence of atherosclerosis is the obstruction of blood flow, since there is a reduction in the cross-sectional area of the artery due to plaque formation, as well as the thickening, hardening and loss of elasticity of the arterial wall. Atherosclerosis can be potentiated by smoking, hypertension and diabetes, among other factors. When a change in lifestyle and statin medications to lower blood cholesterol levels are not sufficient, it is necessary to use a procedure called percutaneous coronary intervention (PCI), commonly known as angioplasty. In this procedure, a tube with a balloon attached is threaded to the obstructed artery, with the balloon being inflated so that the plaque is compressed against the artery wall, eliminating the obstruction. This procedure is often done in conjunction with stenting, in which the stent, a wire mesh tube, is

attached to the outside of the balloon. When the balloon is inflated, the deformed stent remains attached to the artery wall, to help keep the artery unobstructed [11, 12].

The cardiovascular system can be simulated with different levels of detail, from 0D or 1D models to 3D models. The appropriate model varies from case to case, depending on the type of results wanted, for example simple pressure values in the various sections or spatial distributions of velocity, pressure or shear stress. When analyzing blood flow it is usual to use 3D simulations despite needing a larger computational effort because the results obtained are much more detailed, allowing a more complete and complex analysis. On the other hand, less complex models, such as 0D and 1D, are used alone mainly when analyzing blood flow from a macroscopic perspective [13, 14]. Regarding the choice of boundary conditions, the most common and simplest procedure is the use of time-varying, cyclic pressure and velocity/mass flow rate profiles in the inlets and outlets of the computational domain. These profiles are most often obtained using experimental procedures such as doppler ultrasound and pressure wires. A more complex and advanced procedure is to couple the boundaries of the computational domain with 0D and 1D models, which simulate the downstream circulation. This procedure is commonly called the multi-scale modelling of blood flow and its advantage is that it predicts the flow instead of prescribing it [13, 15].

It is known that the walls of the arteries have an elastic behaviour, however, studies have been carried out on blood flow using both rigid and elastic walls. The main reason to model the artery wall as rigid is the resulting simplification, since it is not necessary to solve solids mechanics equations, however, it is accepted that modelling the walls of the arteries as elastic is more appropriate, despite the need for compatibilization between the fluid and solid domains, since this method reproduces more realistically the blood flow behaviour and the wave propagation [16]. Regarding the elasticity of the artery wall, some authors use the linear elastic model, while others use hyperelastic models. The linear elastic model, described by Hooke's Law, assumes a linear relationship between stress and strain and is more appropriate for small or infinitesimal strains, with the deformation dimension significantly lower than the characteristic dimensions of the body. The hyperelastic models describe the relationship between stress and strain as non-linear through a strain energy density function. Experimental results showed that hyperelastic models describe the behaviour of the artery better, but in some cases, the linear elastic model constitutes a reasonable approximation [7, 10, 17, 18, 19].

In general, the numerical methods used to solve fluid-structure interaction problems are divided into two categories, the monolithic approach and the partitioned approach. The monolithic approach is characterized by considering a single domain containing the fluid and the solid, with a single system of equations, therefore the problem is solved simultaneously. The advantages of these methods are that they can ensure better accuracy and can adapt better to a specific problem, while the disadvantages are that it can be much more complex to develop them and they may require a larger computational effort. The partitioned approach, on the other hand, considers two separate computational domains, one for the fluid and one for the solid, each with its own set of equations, numerical methods and mesh. At the interface occurs communication between both domains, with the solid receiving the pressure from the fluid and the fluid receiving displacement from the solid. The Arbitrary Lagrangian-Eulerian (ALE) technique is one of the most used for the interface problem. The main advantage of the partitioned approach is that existing specialized and optimized codes may be used for each domain, having been previously validated and being able to solve complex problems. The inherent difficulty of this approach is the compatibilization of the two domains and their respective solution methodologies, in order to solve the problem efficiently and accurately [20, 21, 22].

## 2. Background

### 2.1. Governing Equations

#### 2.1.1 Fluid Flow

To describe the behaviour of blood flow in the arteries it is necessary to guarantee the conservation of mass and momentum. The conservation of mass results in the continuity equation, while the conservation of momentum is represented by the Navier-Stokes equations for viscous flows. The equation that expresses the conservation of energy is not necessary in the present work, since the flow is isothermal. If blood is modelled as incompressible and the flow is modelled as three-dimensional and unsteady, the continuity, Navier-Stokes and state equations can be written as follows, respectively

$$\nabla \cdot \mathbf{v} = 0 \quad (1)$$

$$\frac{\partial \mathbf{u}}{\partial t} + (\mathbf{v} \cdot \nabla) \mathbf{v} = -\frac{1}{\rho} \nabla P + \nu \nabla^2 \mathbf{v} \quad (2)$$

$$\rho = \text{constant} \quad (3)$$

where  $\mathbf{v}$  is the velocity vector,  $t$  is time,  $\rho$  is the density,  $P$  is the pressure and  $\nu$  is the kinematic viscosity. At the interface, a no-slip condition is considered at all times, guaranteeing that fluid and solid velocities are equal at the interface.

#### 2.1.2 Solid Mechanics

The balance of forces acting on a body is expressed by Cauchy's law,

$$\frac{\partial \sigma_{ij}}{\partial x_j} + F_i = m a_i \quad (4)$$

where  $\sigma_{ij}$  are the components of the stress tensor,  $F_i$  are the body (volume) forces,  $m$  is mass and  $a$  is the acceleration.

The different stress components for a given point are typically represented by the stress tensor, which is written in the form of a matrix. Since this matrix is symmetrical, the tensor can be written in the following vector form,

$$\boldsymbol{\sigma} = [\sigma_{xx} \ \sigma_{yy} \ \sigma_{zz} \ \sigma_{xy} \ \sigma_{xz} \ \sigma_{yz}]^T \quad (5)$$

where  $\sigma_{xx}$ ,  $\sigma_{yy}$  and  $\sigma_{zz}$  are the diagonal terms of the tensor and are called normal stresses, the remaining terms are the shear stresses.

The parameter that allows quantifying the deformation of a body is strain which is related to the displacement field,  $\mathbf{u}$ , and its variation. As is the case with stress, strain at a given point is also represented by a tensor (typically represented in the matrix form), with the following general definition

$$\epsilon_{ij} = \frac{1}{2} \left( \frac{\partial u_i}{\partial x_j} + \frac{\partial u_j}{\partial x_i} - \frac{\partial u_k}{\partial x_i} \frac{\partial u_k}{\partial x_j} \right) \quad (6)$$

with this tensor being used in the cases where there are large deformations. When deformations are very small when compared to the dimensions of the body, the infinitesimal strain simplification may be applied, and thus second order terms are neglected, resulting in

$$\epsilon_{ij} = \frac{1}{2} \left( \frac{\partial u_i}{\partial x_j} + \frac{\partial u_j}{\partial x_i} \right) \quad (7)$$

In order to solve a solid mechanics problem with deformation of the material, additional equations are required, the equations that relate strain and stress. The relation between stress and strain used in most applications is linear, with the Linear Elasticity model being used. If the material is considered isotropic, the stress-strain relation is expressed as follows

$$\sigma_{ij} = \frac{E}{1 + \nu} \left[ \epsilon_{ij} + \frac{\nu}{1 - 2\nu} \epsilon_{kk} \delta_{ij} \right] \quad (8)$$

where  $E$  is Young's modulus,  $\nu$  is poisson's ratio and  $\delta$  is the Kronecker delta. This relation can also be expressed in the matrix form as

$$\boldsymbol{\sigma} = \mathbf{K} \boldsymbol{\epsilon} \quad (9)$$

where  $\mathbf{K}$  is the stiffness matrix that contains the parameters  $E$  and  $\nu$ . In some materials, the relationship between stress and strain is non-linear, requiring the use of a non-linear elasticity model, such as

the Hyperelastic model. In this model, this relationship derives from a strain energy density function,  $W$ . This function is typically expressed in terms of the invariants of the deformation tensor.

$$W = W(I_1, I_2, I_3) \quad (10)$$

From the existing Hyperelastic models, the most well-known are the Neo-Hookean model, the Mooney-Rivlin model, the Ogden model and the Arruda-Boyce model.

In order to simulate damping in a dynamic solids mechanics problem, the Rayleigh damping methodology is widely used. It models the structural response to dynamic efforts using two coefficients, the mass damping coefficient,  $1/\tau_M$  and the stiffness damping coefficient,  $\tau_K$ . The first one damps low frequency oscillations, while the latter damps high frequency oscillations. Both coefficients are used to compute the global damping coefficient, which can be expressed by the following equation

$$\zeta = \frac{1}{2\tau_M \omega} + \frac{\tau_K \omega}{2} \quad (11)$$

where  $\omega$  is the angular frequency. The resulting viscous damping matrix,  $\mathbf{C}$ , can be expressed as

$$\mathbf{C} = \frac{\mathbf{M}}{2\tau_M} + \tau_K \mathbf{K} \quad (12)$$

where  $\mathbf{M}$  is the mass matrix and  $\mathbf{K}$  is the stiffness matrix.

This methodology is often used to simulate viscoelastic or viscoplastic solid behaviour.

## 2.2. Numerical Methods

### 2.2.1 Fluid

Analytical solutions for the fluid governing equations are only possible for a few restricted cases, in the majority of the situations these equations need to be solved numerically. This is the task of computational fluid dynamics (CFD), to obtain an accurate approximation of the studied flows. The fluid flow simulation in this thesis was performed with *Star-CCM+*, which is one of the available CFD commercial softwares. *Star-CCM+* uses the Finite Volume Method (FVM) for the fluid problem, with the original set of partial differential equations being transformed into a system of algebraic equations. To accomplish this, the governing equations are solved over a control volume, or cell, as such they must be expressed in the integral form. Assuming the fluid as incompressible, the continuity equation and the Navier-Stokes equations, respectively, are presented in the integral form as follows

$$\int_V (\nabla \cdot \mathbf{v}) = 0 \quad (13)$$

$$\int_V \rho \frac{\partial \mathbf{v}}{\partial t} dV + \int_V \rho \nabla \cdot (\mathbf{v} \otimes \mathbf{v}) dV = \int_V -\nabla P dV + \int_V \mu \nabla \cdot (\nabla \mathbf{v} + (\nabla \mathbf{v})^T) dV \quad (14)$$

Applying Gauss's divergence theorem to the equations, the divergence terms denoted by  $\nabla \cdot$  are converted in fluxes over the surfaces of the control volume. The theorem is exemplified with the divergence of the velocity.

$$\int_V \nabla \cdot \mathbf{v} dV = \int_S (\mathbf{v} \cdot \mathbf{n}) dS \quad (15)$$

The flux that enters a control volume through a surface is equal to the flux leaving a neighbour control volume through that surface, with the Finite Volume Method being not only globally but also locally conservative. *Star-CCM+* uses first or second order upwind convection schemes. To discretize the temporal term, *Star-CCM+* uses finite differences, more specifically implicit second order finite differences are used. Of the existing algorithms for solving the mass and momentum conservation equations, *Star-CCM+* uses the *SIMPLE* (Semi-Implicit Method for Pressure Linked Equations).

### 2.2.2 Solid

The solid mechanics problem is solved using the commercial software *Abaqus*, with the Finite Element Method (FEM) being used. This method uses the weak formulation of the governing solid equations, which consists in multiplying the differential equations by a test function,  $\varphi$ , and then integrating them over the considered domain.

In this work, the solid mechanics problem is a structural mechanics problem, and as such the coefficient matrix (node connectivity) is called stiffness matrix, containing the elastic properties of the elements and the desired unknowns are the node displacements.

*Abaqus* uses Hilber-Hughes-Taylor time integration, which is second order implicit and unconditionally stable for linear systems. This software solves the system of equations using a direct solver. Since the displacements in this work are significant when compared with the dimensions of the geometry, the resulting equations are non-linear and, as such, the solution requires the update of the stiffness matrix between iterations with Newton methods. If a Full Newton method is used, the stiffness matrix is updated every iteration, but in some cases a Modified Newton method (or quasi-Newton method) is sufficient, where the stiffness matrix is only updated after a given number of iterations or only in the first  $n$  iterations of each time step. In *Abaqus*, from one time step, time is incremented in smaller steps, until the next time step is reached, with the equations being iterated until convergence

for each of these intermediate temporal steps. This time incrementation can be automatic or imposed by the user.

### 2.2.3 Fluid/Solid Coupling, FSI

Given the nature of the studied problem, with pulsatile flow, together with the fact that the artery is a compliant solid that experiences large displacements and with blood and artery having similar densities, the structure is significantly affected by the fluid flow and the opposite is also true, with the fluid flow being affected by the response of the structure. Thus, the coupling between the fluid and the structure is considered a strong coupling, it is necessary to consider a two-way interaction and an implicit coupling scheme must be used. The coupling method used belongs to the partitioned approach to solve FSI problems, with the FVM being used for the fluid problem in *StarCCM+* and the FEM being used for the solid problem in *Abaqus*. In the present work, *StarCCM+* and *Abaqus* were run sequentially with the first one leading the coupling.

### 2.3. Boundary Conditions

Regarding boundary conditions, time-varying mass flow rate at the inlet and time-varying pressure at the outlets was used. In order for the results to be meaningful and realistic, it is necessary to find realistic boundary conditions. These time-varying waveforms were obtained from Kim et al. [7], having a cardiac cycle period of 1 s, and are presented in figure 1. The pressure waveform was obtained for the left circumflex artery and then translated into the other outlets using the relationship between flow and diameter from Zamir et al. [23].

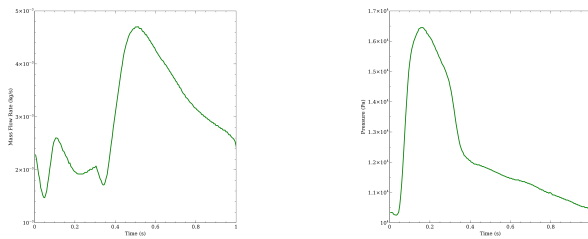


Figure 1: Mass flow rate waveform imposed at the inlet of the model (left) and pressure waveform imposed at the left circumflex artery outlet (right).

Regarding the solid artery wall, it was either modelled as a hyperelastic solid, as a linear elastic solid or as rigid. The outer surface of the wall was subjected to zero relative pressure (ambient pressure) in all cases except one. The geometries of the wall and the fluid were fixed at the extremities at all times.

## 3. Verification and Validation

### 3.1. Verification

A verification study was made for the steady-state case, where the numerical results obtained were compared with the analytical solution of the Hagen-Poiseuille equation. Different types of meshes were tested, as well as increasing number of cells.

Another verification study was performed for the unsteady case, where the numerical results obtained were compared with the analytical solution for pulsatile (Womersley) flow, which is the type of flow that occurs in the arteries. Increasing number of cells, as well as increasing number of time steps per period, were tested.

### 3.2. Validation

A validation study was performed, for the fluid-structure interaction problem of pulsed wave propagation. In order to accomplish this, the results obtained in Janela et al. [24] were reproduced.

## 4. Results

### 4.1. Blood Flow in Left Coronary Arteries in Normal Conditions

#### 4.1.1 Methods

The 3D model obtained from image segmentation was meshed in *Star-CCM+* using polyhedral cells. The resulting mesh contained about 1 million cells. In order to have straight, aligned flow and avoid wave reflections at the inlet and outlets, the mesh was extruded at these regions, with stretching defined so that the last layer has a thickness five times larger than the first layer. The model is represented in figure 2, where the branches are also identified. The inlet corresponds to the LCA and the outlets correspond to the beginning of the LCX, three LAD branches, LAD1, LAD2 and LAD3 and two small LAD branches, SB1 and SB2.

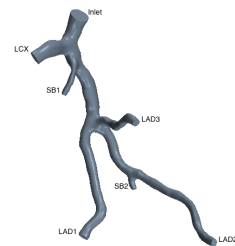


Figure 2: Geometry of the arteries and identification of the branches

The artery wall geometry was generated by extruding the wall of the fluid model, resulting in a 1 mm thick artery wall model. In this simulation, the finite element mesh for the solid artery wall was constructed in *Abaqus* with around 300,000 quadratic tetrahedral elements.

Blood was modelled as a Newtonian, incompressible fluid with  $\rho = 1060 \text{ kg/m}^3$  and  $\mu = 0.004 \text{ Pa}\cdot\text{s}$

and blood flow was modelled as three dimensional, laminar and unsteady in all simulations in the present section. The fluid boundary conditions used are the mass flow inlet waveform and the pressure outlet waveforms specified in the previous section. The artery wall was modelled with the nine parameter Mooney-Rivlin isotropic hyperelastic model, with parameters  $c_{10} = 0.070$ ,  $c_{20} = 3.2$ ,  $c_{21} = 0.0716$  MPa, remaining  $c_{ij} = 0$  MPa and  $d = 1 \times 10^{-5}$  Pa<sup>-1</sup>, obtained from Torii et al. [10]. The nine parameter Mooney-Rivlin strain energy density function is

$$\begin{aligned}
W = & c_{10} (\bar{I}_1 - 3) + c_{01} (\bar{I}_2 - 3) + c_{20} (\bar{I}_1 - 3)^2 \\
& + c_{11} (\bar{I}_1 - 3) (\bar{I}_2 - 3) + c_{02} (\bar{I}_2 - 3)^2 + c_{30} (\bar{I}_1 - 3)^2 \\
& + c_{21} (\bar{I}_1 - 3)^2 (\bar{I}_2 - 3) + c_{12} (\bar{I}_1 - 3) (\bar{I}_2 - 3)^2 \\
& + c_{03} (\bar{I}_2 - 3)^3 + \frac{1}{d} (J - 1)^2 \quad (16)
\end{aligned}$$

where  $\bar{I}_1$  and  $\bar{I}_2$  are the first and second deviatoric strain invariants and  $J$  is the determinant of the elastic deformation gradient tensor. The artery wall density was considered to be  $\rho = 1000$  kg/m<sup>3</sup> and the Rayleigh damping methodology was used with a stiffness damping coefficient  $\tau_K = 0.5$  s.

The pressure, WSS, velocity and displacement distributions are analyzed in three specific times of the cardiac cycle, corresponding to the maximum pressure value,  $t_1 = 0.165$  s, maximum mass flow rate value,  $t_2 = 0.515$  s, and the end of the cycle,  $t_3 = 1$  s.

#### 4.1.2 Results

The distribution of pressure in the fluid domain is analyzed for the three specific times of the cycle, mentioned above. Figure 3 shows that in  $t_1$  pressure is much higher than in  $t_2$ , where mass flow rate is maximum and in the end of the cycle,  $t_3$ . In all the considered times, the maximum pressure value is located in the region where the LCX and SB1 branch begins. This is explained by the fact that blood flows from the inlet with high velocity and the flow streamlines experience large deflections when leaving the main artery and entering the branches, which causes forces and consequently higher pressure on the wall in that particular region. Pressure is locally higher in other branching regions, as is the case of the branching of the LAD artery into LAD1, LAD2 and LAD3 and of the branching of LAD2 into SB2.

Velocity contours were analyzed in different cross section of the arteries, with emphasis on the beginning of the branches. The shape of the velocity contours is not exactly parabolic due to the curvature in the artery and to the fact that the artery does not have an exactly circular section. Figure 4 shows the velocity contour in the beginning of the

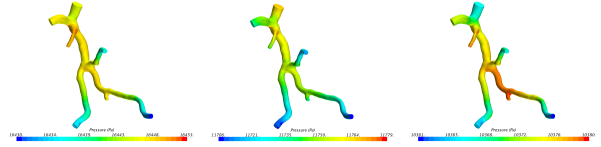


Figure 3: Pressure distribution in normal arteries at times  $t_1$  (left),  $t_2$  (middle) and  $t_3$  (right).

LCX branch, the most affected by the deflection caused by the branching, in times  $t_1$ ,  $t_2$  and  $t_3$ . It is possible to observe that the velocity magnitude is much higher in  $t_2$  than in the remaining times, due to the fact that the mass flow rate being imposed at the inlet in that time corresponds to the maximum value in the cycle. The velocity contours for a given section are similar in all the considered times.

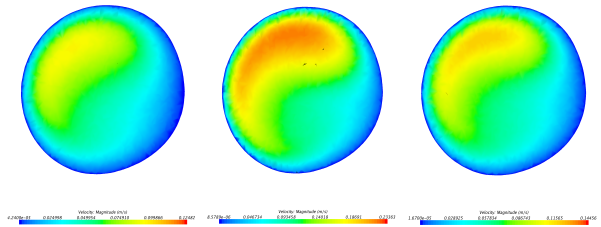


Figure 4: Velocity contour in the beginning of the LCX branch at times  $t_1$  (left),  $t_2$  (middle) and  $t_3$  (right).

In figure 5, it is possible to observe that the waveform representing the evolution of the average WSS on the wall follows the shape of the mass flow rate waveform imposed at the inlet. This is expected, since mass flow rate is proportional to the velocity and WSS is computed from the velocity field, more precisely from the velocity derivative in the direction perpendicular to the wall. The maximum WSS waveform follows the basic shape of the mass flow rate waveform. The obtained results are close to those obtained in the literature [7]. The WSS distribution in the three specified times,  $t_1$ ,  $t_2$  and  $t_3$ , is presented in figure 6. The maximum WSS values are located in the same regions as the maximum pressure values, near branching. The same phenomenon that leads to the existence of high pressures also causes high WSS values. Regions with lower WSS values, identified by dark blue colour, are in theory regions where it is more likely that the deposition of atherosclerotic plaques occurs.

The temporal evolution of the average and maximum artery displacement within one cardiac cycle is displayed in figure 7. It is important to notice that, since a new cyclic equilibrium was obtained, the displacement lowest value is different than zero. The average and maximum displacement waveforms are similar, having different am-

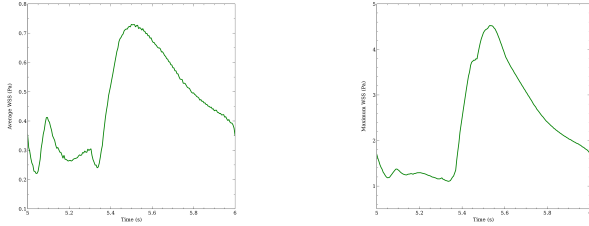


Figure 5: Temporal evolution of average and maximum WSS in arteries in normal conditions.

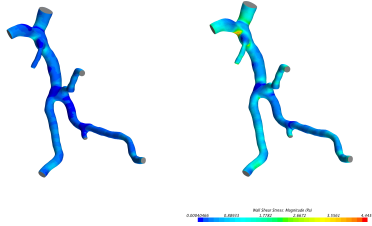


Figure 6: WSS distribution in the arteries at times  $t_1$  (left),  $t_2$  (middle) and  $t_3$  (right).

plitudes. The displacement waveform follows the pressure waveforms (figure 1) with delay, which is in part caused by the considered damping. In figure 8, the displacement distribution is presented on the left for  $t_1$ . The spatial relative displacement distribution between different times of the cardiac cycle has minimal variation, which means that displacement varies approximately the same amount in every point of the domain between different times. In figure 8 (right), a comparison between the deformed (green, with scale factor of 7.5) and undeformed (red) configurations of the artery ( $t_1$ ) is made in the LAD branches, where it can be seen that, using a hyperelastic model for the artery, there is not only variation of diameter, but also an oscillatory movement of the artery due to the blood flow. During the cycle, the oscillatory displacement is larger than the displacement due to the variation of the diameter.

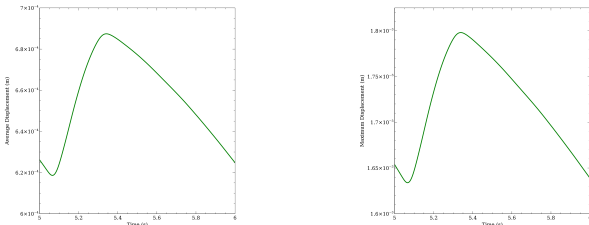


Figure 7: Temporal evolution of the average and maximum artery displacement over the cardiac cycle in arteries in normal conditions.



Figure 8: Displacement distribution in normal arteries in  $t = t_1$  (left) and comparison between deformed and undeformed configurations (right).

## 4.2. Blood Flow in Stenosed Left Coronary Arteries

### 4.2.1 Methods

In order to simulate stenosed arteries, the diameter was progressively reduced in a certain region of the artery, with a maximum reduction of 50%, which corresponds to about 75% reduction of the cross-sectional area. This value is considered the limit for critical obstruction that can lead to serious complications, according to the literature [25, 26]. The stenosed region of the coronary model is shown in figure 9



Figure 9: Stenosed region

The fluid and the solid were modelled exactly the same way as was done in the section above.

### 4.2.2 Results

In this work, mass flow rate is imposed at the inlet and pressure is imposed at the outlets. In the case of stenosed arteries, due to the local reduction of cross-sectional area in the stenosed region, in order to be able to meet the mass flow rate that is imposed at the inlet, a higher pressure must be verified at the inlet. This is showed in table 1, with the pressure differences between the inlet and LAD2 (the outlets have the same pressure value imposed in normal and stenosed cases) for times  $t_1$ ,  $t_2$  and  $t_3$  being presented for normal arteries and stenosed arteries. Stenosed arteries present higher pressure differences in all considered times, with the difference in  $t_2$  being significantly higher. In a computational simulation, with the mass flow rate imposed at the inlet, the higher pressure verified at the inlet is a natural consequence. However, in real arteries, the human body may be able to adapt until a certain degree of stenosis, imposing higher pressure at the inlet or reducing the resistance in the capillaries, but when a critical stenosis is reached, it may not be possible to further increase the pressure difference between the inlet and the outlets, which inevitably leads to a reduction of the flow entering the arteries.

Condition	$t_1$	$t_2$	$t_3$
Normal	23.14 Pa	84.27 Pa	29.46 Pa
Stenosed	25.78 Pa	93.83 Pa	32.11 Pa

Table 1: Pressure difference between Inlet and LAD2 for  $t_1$ ,  $t_2$  and  $t_3$

The velocity contours were analyzed in the stenosed region, with the velocity contours at times  $t_1$ ,  $t_2$  and  $t_3$  at the end of the stenosis (downstream) presented in figure 10. In this figure, it is possible to observe low velocity recirculation zones at the bottom right and top right of the section for all considered times and also at the left side of the section for  $t_2$ . These recirculation zones can be seen downstream of the maximal stenosis section, in figure 11, where the streamlines in the stenosed region are presented for  $t_2$ . A possible consequence of the existence of low velocity recirculation zones in this region is the downstream spreading of the stenosis, since these zones are where plaque deposition is most likely to occur. In figure 11 it is also possible to observe the 3D nature of the flow in that region.

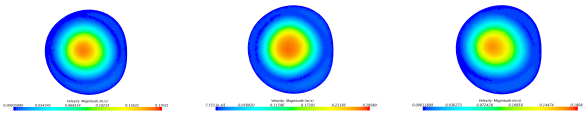


Figure 10: Velocity contours at the end of the stenosis at times  $t_1$ ,  $t_2$  and  $t_3$

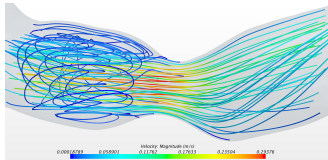


Figure 11: Streamlines in the stenosed region for  $t = t_2$

### 4.3. Blood Flow in Stented Left Coronary Arteries

#### 4.3.1 Methods

The presence of the stent was simulated with a realistic stent geometry contacting the arterial wall. The stent geometry used is presented in figure 12.



Figure 12: Stent geometry

The modelling of the fluid and solid artery do-

main was performed with the same specifications that were described in the previous sections.

The stent geometry was meshed in *Abaqus*, resulting in about 40,000 FEM quadratic tetrahedral elements. The surface of the stent was tied to the contacting artery surface. The stent was modelled as stainless steel, specifically the 316L alloy, with a Young's modulus of 193 GPa, a Poisson's ratio of 0.27 and a density of 8000 kg/m<sup>3</sup>, assumed as a linear isotropic material.

#### 4.3.2 Results

The global pressure distribution in stented left coronary arteries is similar to the pressure distribution in normal arteries, with the maximum pressure values being also located in branching regions for the reasons explained in the analysis of pressure distribution in normal arteries. However, in the region where the stent is placed, the local pressure distribution in the stented arteries is significantly different from that in normal arteries. Figure 13 shows the local pressure distribution in a longitudinal section across the region where the stent is placed, in  $t_2$ . It can be seen that, due to the obstruction caused by the stent geometry in the flow, pressure has a local maximum value right before the stent wire and a local minimum value right after the stent. This is due to the deflection of the streamlines in order to avoid the obstruction.

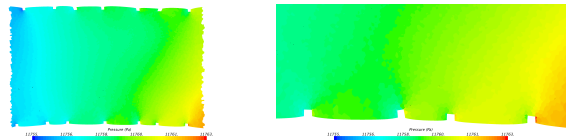


Figure 13: Local pressure distribution ( $t=t_2$ ) in the stented region (left) and a zoom near the wall (right).

In figure 14, it is possible to see the streamlines in the region where the stent is placed (which corresponds to the stenosed region from the previous section) in  $t_2$ . Once again, the three-dimensional nature of the flow is visible. The flow near the centre of the artery section in the stented region is similar to the one verified in normal arteries. However, the flow near the wall is altered in stented arteries, due to the deflection imposed on the streamlines by the geometry of the stent. These deflections are visible in the image on the right, which shows a zoomed plane near the wall.

Global WSS distribution in stented arteries is similar to the one obtained in normal arteries. However, in the artery section where the stent is placed, the local WSS distribution shows differences when compared to the case of normal arteries. The local WSS distribution in the region where the stent

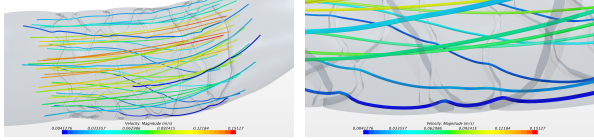


Figure 14: Streamlines in the stented region (left) and a zoom near the wall (right).

is placed is shown in figure 15. It is possible to observe that WSS values are higher in the lower surface of the stent, which is caused by the deflection imposed on the current lines, in order to avoid the geometry of the stent. Due to this deflection, the velocity derivative near the wall presents high values, which leads to high WSS values.

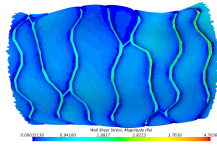


Figure 15: Local WSS distribution in the stented region.

The average and maximum displacement evolution with time in stented left coronary arteries is presented in figure 16. It can be seen for both average and maximum WSS curves that the displacement base value is lower for stented arteries and that the displacement variation (difference between maximum and minimum value in each curve) is also lower, when compared to normal arteries. This is expected, since the permanent contact between the stent and the artery in a specific region leads to an increase in the effective stiffness of the artery locally.

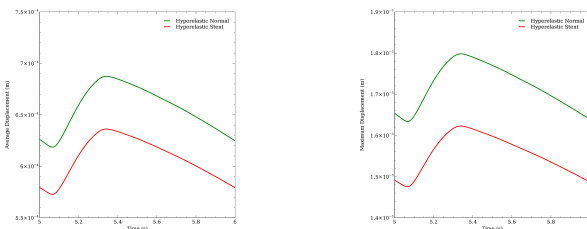


Figure 16: Temporal evolution of average (left) and maximum (right) displacement in stented arteries.

## 5. Conclusions

In the present work, an analysis of blood flow in the left coronary arteries was made. The basic geometry used to model the arteries was obtained using medical imaging segmentation. Three different artery conditions were simulated, normal, stenosed and stented.

In the analysis of blood flow in normal left coronary arteries, it was found that the branching regions, associated with geometry curvature, lead to significant changes in local velocity profiles. The deflection imposed on the streamlines in these regions leads to the occurrence of the maximum values of pressure and wall shear stress in the domain. It was verified that the variation of displacement during a cardiac cycle is one order of magnitude below the dimension of the diameter, having significant implications in the blood flow. In this sense, a rigid wall approach may not be appropriate.

Regarding stenosed arteries, it was found that blood flow is altered significantly in the stenosis region, due to the cross-sectional area variation, together with curvature of the geometry. The maximum WSS value verified in this case was significantly higher than the one verified in normal arteries. One of the main consequences of the obstruction caused by the stenosis is the existence of low velocity recirculation zones immediately downstream, increasing the risk of stenosis spreading. It was also verified that there is an increase in the pressure gradient between the inlet and the outlets, which may not be achievable in reality, leading to a consequent decrease in the flow rate in the coronary arteries.

Lastly, with regard to stented arteries it was concluded that the stent presence influences blood flow locally, due to the physical obstruction that it constitutes near the wall. This influence is more significant near the wall, where the pressure and WSS distributions are affected. It was found that, while the streamlines undergo deflections near the wall, there are no significant changes in the flow in the central section of the artery.

## References

- [1] Haidong Wang et al. Global, regional, and national life expectancy, all-cause mortality, and cause-specific mortality for 249 causes of death, 1980-2015: a systematic analysis for the Global Burden of Disease Study 2015. *The Lancet*, 388(10053):1459–1544, 2016.
- [2] Bin He et al. Grand challenges in interfacing engineering with life sciences and medicine. *IEEE Transactions on Biomedical Engineering*, 60(3):589–598, 2013.
- [3] Byoung-Kwon Lee. Computational Fluid Dynamics in Cardiovascular Disease. *Korean Circulation Journal*, 41(8):423–430, 2011.
- [4] Paul D Morris et al. Computational fluid dynamics modelling in cardiovascular medicine. *Heart (British Cardiac Society)*, pages heartjnl-2015-308044–, 2015.

- [5] C.A. Taylor and J.D. Humphrey. Open problems in computational vascular biomechanics: Hemodynamics and arterial wall mechanics. *Computer Methods in Applied Mechanics and Engineering*, 198(45-46):3514–3523, sep 2009.
- [6] Y. C. Fung. *Biomechanics: Circulation*. Springer, second edition, 1997.
- [7] H. J. Kim, I. E. Vignon-Clementel, J. S. Coogan, C. A. Figueroa, K. E. Jansen, and C. A. Taylor. Patient-Specific Modeling of Blood Flow and Pressure in Human Coronary Arteries. *Annals of Biomedical Engineering*, 38(10):3195–3209, oct 2010.
- [8] Jos A. E. Spaan. *Coronary Blood Flow: Mechanics, Distribution, And Control*. Springer Science+Business Media Dordrecht, 1st edition, 1991.
- [9] Valentin Fuster, Richard A. Walsh, and James C. Fang. *Hurst's The Heart: Manual of Cardiology*. McGraw-Hill, thirteenth edition, 2013.
- [10] Ryo Torii et al. Fluid-structure interaction analysis of a patient-specific right coronary artery with physiological velocity and pressure waveforms. *Communications in Numerical Methods in Engineering*, 25(5):565–580, may 2009.
- [11] David Willerson, James T., R. Holmes, Jr. *Coronary Artery Disease*. Cardiovascular Medicine. Springer London, 2015.
- [12] L. Maximilian Buja and James T. Willerson. The role of coronary artery lesions in ischemic heart disease: Insights from recent clinicopathologic, coronary arteriographic, and experimental studies. *Human Pathology*, 18(5):451–461, 1987.
- [13] Jack Lee and Nicolas P. Smith. The multi-scale modelling of coronary blood flow. *Annals of Biomedical Engineering*, 40(11):2399–2413, 2012.
- [14] Nan Xiao, Jordi Alastruey, and C. Alberto Figueroa. A systematic comparison between 1-D and 3-D hemodynamics in compliant arterial models. *International Journal for Numerical Methods in Biomedical Engineering*, 30(2):204–231, feb 2014.
- [15] Irene E. Vignon-Clementel, C. Alberto Figueroa, Kenneth E. Jansen, and Charles A. Taylor. Outflow boundary conditions for three-dimensional finite element modeling of blood flow and pressure in arteries. *Computer Methods in Applied Mechanics and Engineering*, 195(29-32):3776–3796, 2006.
- [16] Davide Ambrosi, Alfio Quarteroni, and Gianluigi Rozza. *Modeling of Physiological Flows*. Springer-Verlag Italia, 2012.
- [17] Y. C. Fung. *Biomechanics: Mechanical Properties of Living Tissues*. Springer, second edition, 1993.
- [18] Alvaro Valencia and Francisco Solis. Blood flow dynamics and arterial wall interaction in a saccular aneurysm model of the basilar artery. *Computers and Structures*, 84(21):1326–1337, 2006.
- [19] C. Lally, A. J. Reid, and Patrick J. Prendergast. Elastic behavior of porcine coronary artery tissue under uniaxial and equibiaxial tension. *Annals of Biomedical Engineering*, 32(10):1355–1364, 2004.
- [20] Gene Hou, Jin Wang, and Anita Layton. Numerical methods for fluid-structure interaction - A review. *Communications in Computational Physics*, 12(2):337–377, 2012.
- [21] Jean-Francois Sigrist. *Fluid-Structure Interaction: An Introduction to Finite Element Coupling*. Wiley, 2015.
- [22] Mhamed Souli and David J. Benson. *Arbitrary Lagrangian-Eulerian and Fluid-Structure Interaction*. Wiley-ISTE, 2013.
- [23] Mair Zamir, Paula Sinclair, and Thomas H. Wonnacott. Relation between diameter and flow in major branches of the arch of the aorta. *Journal of Biomechanics*, 25(11):1303–1310, 1992.
- [24] João Janela, Alexandra Moura, and Adélia Sequeira. A 3D non-Newtonian fluid-structure interaction model for blood flow in arteries. *Journal of Computational and Applied Mathematics*, 234(9):2783–2791, 2010.
- [25] P J Harris et al. The prognostic significance of 50% coronary stenosis in medically treated patients with coronary artery disease. *Circulation*, 62(2):240–248, 1980.
- [26] Gary W Burggraf and J. O. Parker. Prognosis in coronary artery disease. Angiographic, hemodynamic, and clinical factors. *Circulation*, 51(1):146–156, 1975.